SCIENCE CHINA
Earth Sciences

•RESEARCH PAPER•

October 2021 Vol.64 No.10: 1607–1618
https://doi.org/10.1007/s11430-020-9758-9

Influences of three oceans on record-breaking rainfall over the Yangtze River Valley in June 2020

Jiayu ZHENG[1,2,3,4] & Chunzai WANG[1,3,4*]

[1] *State Key Laboratory of Tropical Oceanography, South China Sea Institute of Oceanology, Chinese Academy of Sciences, Guangzhou 510301, China;*
[2] *State Key Laboratory of Numerical Modeling for Atmospheric Sciences and Geophysical Fluid Dynamics, Institute of Atmospheric Physics, Chinese Academy of Sciences, Beijing 100029, China;*
[3] *Southern Marine Science and Engineering Guangdong Laboratory (Guangzhou), Guangzhou 511458, China;*
[4] *Innovation Academy of South China Sea Ecology and Environmental Engineering, Chinese Academy of Sciences, Guangzhou 510301, China*

Received December 18, 2020; revised February 4, 2021; accepted March 16, 2021; published online March 19, 2021

Abstract The rainfall over the Yangtze River Valley (YRV) in June 2020 broke the record since 1979. Here we show that all three oceans of the Pacific, Indian and Atlantic Oceans contribute to the YRV rainfall in June 2020, but the Atlantic plays a dominant role. The sea surface temperature (SST) anomalies in three oceans are associated with the two vorticity anomalies: negative 200-hPa relative vorticity anomalies over North China (NC) and negative 850-hPa relative vorticity anomalies in the South China Sea (SCS). The rainfall anomalies in the YRV are mainly controlled by atmospheric process associated with the NC vorticity. The positive SST anomalies in May over the western North Atlantic induce positive geopotential height anomalies in June over the mid-latitude North Atlantic, which affect the rainfall anomalies in the YRV by changing the NC vorticity via Atlantic-induced atmospheric wave train across Europe. The Indian Ocean and tropical North Atlantic, as capacitors of Pacific El Niño events in the preceding winter, affect the SCS vorticity associated with the anomalous anticyclone over the SCS and also facilitate the YRV rainfall by providing favorable moisture conditions. This study suggests that the May SST over the western North Atlantic is a good predictor of June rainfall anomalies in the YRV and highlights the important impacts of three-ocean SSTs on extreme weather and climate events in China.

Keywords Rainfall, Yangtze River Valley, Western North Atlantic, Three oceans

Citation: Zheng J, Wang C. 2021. Influences of three oceans on record-breaking rainfall over the Yangtze River Valley in June 2020. Science China Earth Sciences, 64(10): 1607–1618, https://doi.org/10.1007/s11430-020-9758-9

1. Introduction

Rainfall is important for agricultural planning, water supply, industrial production and so on. However, torrential rain can cause widespread inland flooding, which often causes large economic losses and casualties in the affected areas. China is located in the East Asian monsoon region, and many studies have focused on summer rainfall variations in China and the relationship with the East Asian summer monsoon, western Pacific subtropical high (WPSH), Pacific El Niño-Southern Oscillation (ENSO) events, Indian Ocean sea surface temperature (SST), North Atlantic Oscillation, and Southern Hemisphere Annular Mode (Li and Zeng, 2002; Lu, 2002; Nan and Li, 2003; Xie et al., 2009; Wu et al., 2009; Ding et al., 2010; Chen et al., 2019; Liu et al., 2020).

For June rainfall in China, Wang and Gu (2016) showed that two record-breaking rainfalls in late June of 2015 were caused by El Niño-like SST pattern and two mid-latitude

* Corresponding author (email: cwang@scsio.ac.cn)

blockings. Sun et al. (2018) found that the extremities of the atmospheric circulation over south Europe and Australian high led to record-breaking rainfall over South China in June 2017. Yuan et al. (2019) indicated that the major monsoon rainbelt was located in South China (the Yangtze River Valley (YRV)) in the early rainy season of May–June (late rainy season of July–August), and the variations in the South China precipitation in the early and late rainy seasons were controlled by different types of SST patterns in the tropical Indian and Pacific Oceans. These results suggest that both tropical and subtropical factors play important roles in the rainfall variations in China, and thus research on rainfall variations in China is warranted.

In June 2020, the rainfall in the YRV is very intense. The China Meteorological Administration shows that there are large-scale heavy rainfall processes in the YRV, which lead to flood disasters in many provinces of China. As of June 28, the People's Daily Online reports that there are more than 12 million people affected by disasters related to this torrential rain, with deaths or disappearances of 78 persons and a direct economic loss of more than 25 billion CNY. Figure 1a and 1b shows the rainfall anomalies over the YRV in June 2020 relative to the climatological mean of 1981–2010 using the CMAP (Climate Prediction Center Merged Analysis of Precipitation) and PREC/L (Precipitation Reconstruction over Land) datasets. Strong positive rainfall anomalies cover the YRV in both datasets. Besides, the rainfall belt in June 2020 migrates northward to the YRV in comparison with that for the climatological mean (Figure S1, http://link.springer.com). To quantitate the rainfall variations in the YRV, the YRV rainfall index is calculated as the average rainfall in the YRV region (110°–122°E, 30°–34°N). As shown in Figure 1c, the standardized YRV rainfall index in June 2020 is greater than 3.0, which broke the intensity record since 1979. In addition, the detrended YRV rainfall index in June 2020 is still the highest (Figure 1d), and the intensity of the El Niño event in the preceding winter is not very strong (see Figure S2). These results suggest that we can not simply attribute this heavy rainfall to the Pacific El Niño event or global warming.

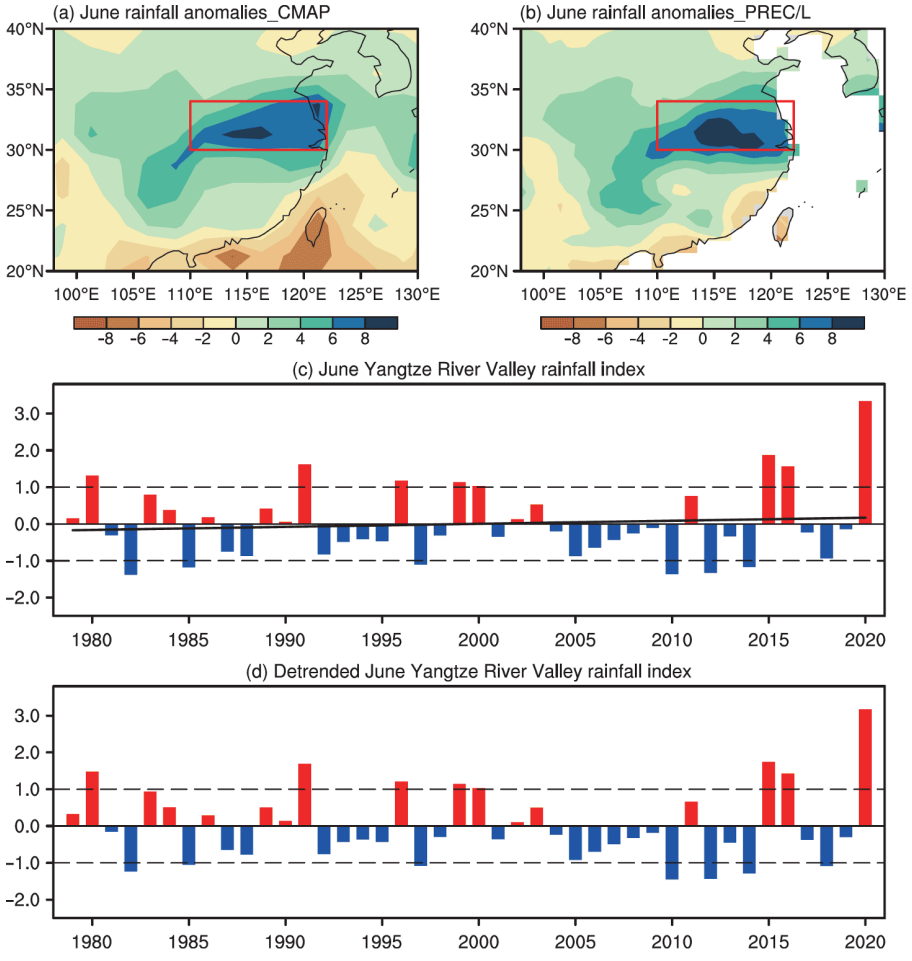

Figure 1 Rainfall anomalies over the Yangtze River Valley (YRV) in June 2020. (a) and (b) Rainfall anomalies (unit: mm day^{-1}) over the YRV in June 2020 using the CMAP dataset and PREC/L dataset. Red rectangles denote the YRV region (110°–122°E, 30°–34°N). (c) Standardized time series of the June YRV rainfall index (bar charts) using the CMAP dataset. The YRV rainfall index is defined as the average rainfall over the YRV region. The black line denotes the linear trend of the time series. (d) As in (c) but for detrended time series of the June YRV rainfall index.

Recently, Takaya et al. (2020) suggest that Indian Ocean warming contributes to enhanced Meiyu-Baiu rainfall over Japan and central China in June–July 2020, and the warm Indian Ocean condition is originated from the super Indian Ocean dipole in 2019. Liu et al. (2020) indicate that record-breaking Meiyu rainfall around the YRV in 2020 is regulated by the subseasonal phase transition of the North Atlantic Oscillation. However, the rainfall in June–July 2020 is taken as a whole in Takaya et al. (2020), while Meiyu rainfall is investigated on a submonth time scales (12–25 June and 30 June–13 July) in Liu et al. (2020). Wang (2019) indicates that interactions among the Pacific, Atlantic and Indian Oceans can initiate and/or modulate climate variability. The present paper focuses on processes associated with the enhanced rainfall in June 2020 on time scales longer than a month, and emphasizes the influences of three-oceans (the Pacific, Indian and Atlantic Oceans) on the YRV rainfall in June 2020.

2. Datasets and methodology

The precipitation datasets we used in this study are the CMAP dataset (Xie and Arkin, 1997) and U.S. National Oceanic and Atmospheric Administration's (NOAA's) PREC/L dataset on a 1.0°×1.0° grid (Chen et al., 2002). The atmospheric dataset employed in this study is the U.S. National Centers for the Environmental Prediction/National Center for Atmospheric Research (NCEP/NCAR) reanalysis I, which includes geopotential height (GPH), winds, specific humidity, and surface pressure on a 2.5°×2.5° grid (Kalnay et al., 1996). For the SST dataset, we use the NOAA Extended Reconstructed Sea Surface Temperature (SST) V5 (Huang et al., 2017).

The analyses are performed for the 1979–2020 period, and the climatological mean is defined as the mean over the 1981–2010 period. To reduce the effect of global warming, a linear trend is removed before the analyses. The atmospheric wave activities in this study are described by using wave activity flux derived by Takaya and Nakamura (2001). To get a better structure of atmospheric wave activities, zonal wavenumbers of 1 to 5 of stream function anomalies are chosen to calculate wave activity flux.

3. Results

3.1 Atmospheric circulation anomalies associated with enhanced rainfall in the YRV

To detect the atmospheric circulation anomalies associated with the enhanced rainfall, Figure 2 shows the atmospheric circulation anomalies and moisture flux anomalies around the YRV in June 2020. At 850 hPa, an anomalous anticyclone is located over the western North Pacific (Figure 2a). This anomalous anticyclone can transport more moisture to the YRV (Figure 2e and 2f), and lead to positive rainfall anomalies in the YRV (Figure S3). At 500 hPa, Figure 2b shows that there are positive GPH anomalies located over East China. The range of the WPSH and the ridge of the WPSH for June 2020 and the climatological mean are also shown in Figure 2b. Upon comparison with the climatological mean, the WPSH strengthens and extends westward, and the ridge and northwest flank of the WPSH are located further north in June 2020. At 200 hPa, positive GPH anomalies are located in the north of China. Besides, the South Asian High (SAH) strengthens and extends eastward, and the ridge and northeast flank of the SAH are further north in June 2020 (Figure 2c). The western extension of the WPSH in the lower troposphere and eastern extension of the SAH in the upper troposphere favor abundant Meiyu rainfall in East Asia (Ding and Chan, 2005; Ding et al., 2020). However, it should also be noted that both the ridge of the WPSH and the SAH show a northward shift in June 2020. On the other hand, there are a strong downward vertical movement over the western North Pacific and a strong upward movement over the northwest flank of the WPSH (Figure 2d), which lead to the divergence of water vapor over the YRV (Figure 2e). Overall, the low-level anomalous anticyclone over the western North Pacific and the northward shift of the WPSH can transport more water vapor to the YRV and result in positive rainfall anomalies there.

In previous studies, relative vorticity was used to measure the variations in the WPSH (Yang and Sun, 2005; Lu et al., 2008). To obtain a better understanding of the atmospheric circulation anomalies contributing to the record-breaking rainfall in June 2020, Figure 3 presents relative vorticity anomalies in June 2020. At 200 hPa, negative relative vorticity anomalies are located in North China (NC). At 500 hPa, in additional to negative relative vorticity anomalies near the YRV, another negative relative vorticity is located in the northern South China Sea (SCS). At 850 hPa, negative relative vorticity anomalies are located in the region from the SCS to South China, which is consistent with the anticyclonic anomalies in Figure 2a. Figure 3d shows that negative relative vorticity at 200 hPa extends southward and downward and merges with the negative relative vorticity at low-levels, suggesting that the NC vorticity may be related to the relative vorticity anomalies at low-levels.

Based on the relative vorticity anomalies in June 2020, the NC vorticity is defined as 200-hPa relative vorticity in the NC region (102.5°–132.5°E, 27.5°–40°N). Figure 3e presents 850-hPa relative vorticity anomalies regressed onto the reversed NC vorticity. For the convenience of comparison with the observed anomalies in June 2020, the sign of the NC vorticity is reversed. The 850-hPa relative vorticity anomalies in South China is related to the 200-hPa NC vorticity, but the negative 850-hPa relative vorticity anomalies in the SCS

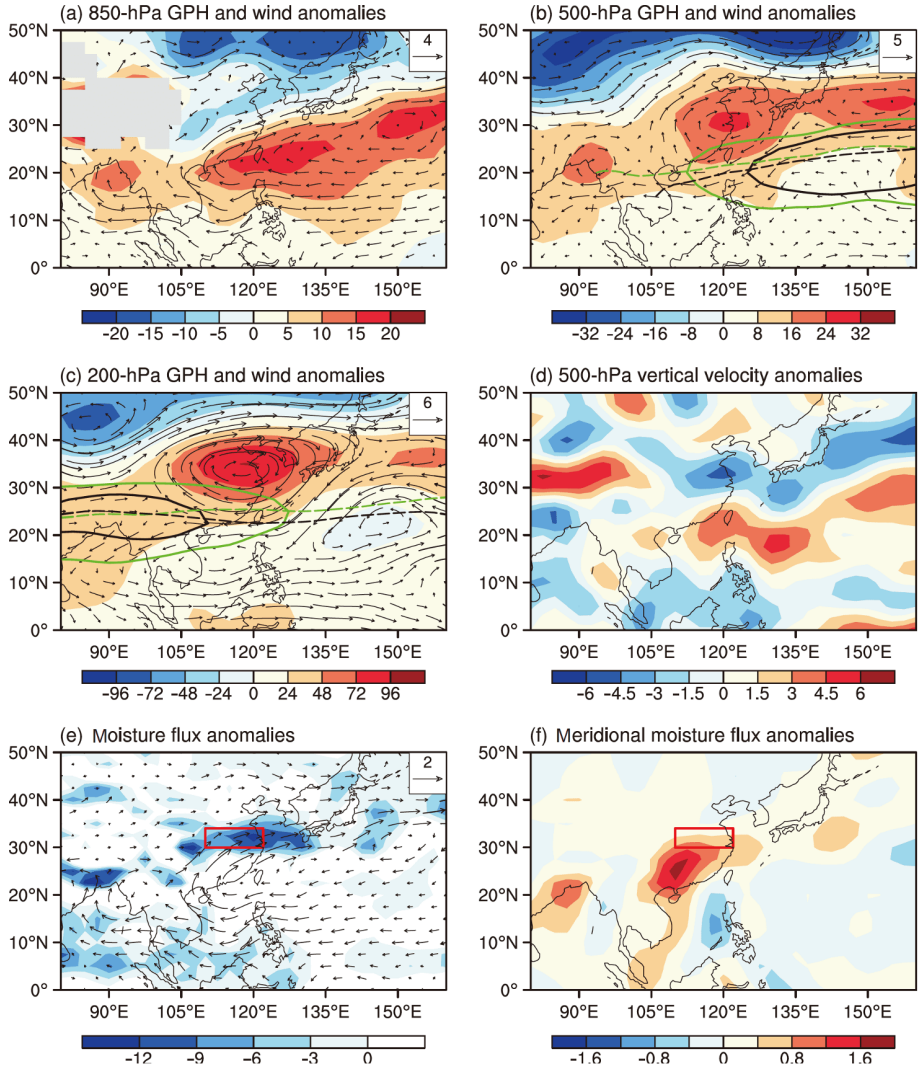

Figure 2 Atmospheric circulation and moisture flux anomalies in June 2020. (a) 850-hPa GPH (shading, unit: gpm) and wind anomalies (vectors, unit: m s^{-1}) in June 2020. (b) As in (a) but for 500-hPa. The solid lines represent the range of the WPSH denoted by the 5880-gpm line, and the dashed lines represent the ridge of the WPSH. Green (black) lines denote the WPSH and ridge of the WPSH for June 2020 (climatological mean). (c) As in (a) but for 200-hPa. The solid lines represent the range of the South Asian high (SAH, denoted by the 12520-gpm line), and the dashed lines represent the ridge of the SAH. Green (black) lines denote the SAH and ridge of the SAH for June 2020 (climatological mean). (d) 500-hPa vertical velocity anomalies (negative values denote upward motion, unit: 10^{-2} Pa s^{-1}) in June 2020. (e) Column-integrated moisture flux anomalies (vectors, unit: 10^{2} kg m^{-1} s^{-1}) and its divergence anomalies (shading, unit: 10^{-5} kg m^{-2} s^{-1}, negative values denote convergence of moisture flux) in June 2020. (f) Meridional moisture flux anomalies (unit: 10^{2} kg m^{-1} s^{-1}) in June 2020. Red rectangles in (e) and (f) denote the YRV region.

are insignificantly correlated with the NC vorticity (Figure 3c and 3e). Because of these reasons, another vorticity index, which is termed the SCS vorticity, is defined as 850-hPa relative vorticity in the region (110°–117.5°E, 10°–20°N). As shown in Figure 3f, both the NC vorticity and the SCS vorticity are on their negative phases in June 2020, and the NC vorticity breaks the record since 1979. We hypothesize that this distinguished structure of atmospheric circulation (co-existence of negative SCS vorticity in the lower troposphere and negative NC vorticity in the upper troposphere) may be responsible for the record-breaking rainfall over the YRV in June 2020.

To further investigate the relationship between the SCS (NC) vorticity and rainfall in the YRV, Figure 4 shows the 850-hPa wind anomalies, moisture flux anomalies and rainfall anomalies regressed onto the reversed SCS vorticity and reversed NC vorticity. When the SCS vorticity is negative, there are anticyclonic circulation anomalies and negative 850-hPa relative vorticity anomalies in the SCS and the Philippine Sea, which can transport more water vapor from the SCS to South China and contribute to positive rainfall anomalies in South China (Figure 4a and 4c). When the NC vorticity is negative, there are anticyclonic circulation anomalies and negative 850-hPa relative vorticity anomalies in South China and north of the Philippine Sea, which can transport more water vapor from South China to the YRV and contribute to positive rainfall anomalies in the YRV (Figure 4b and 4d). Notably, meridional moisture transportation is

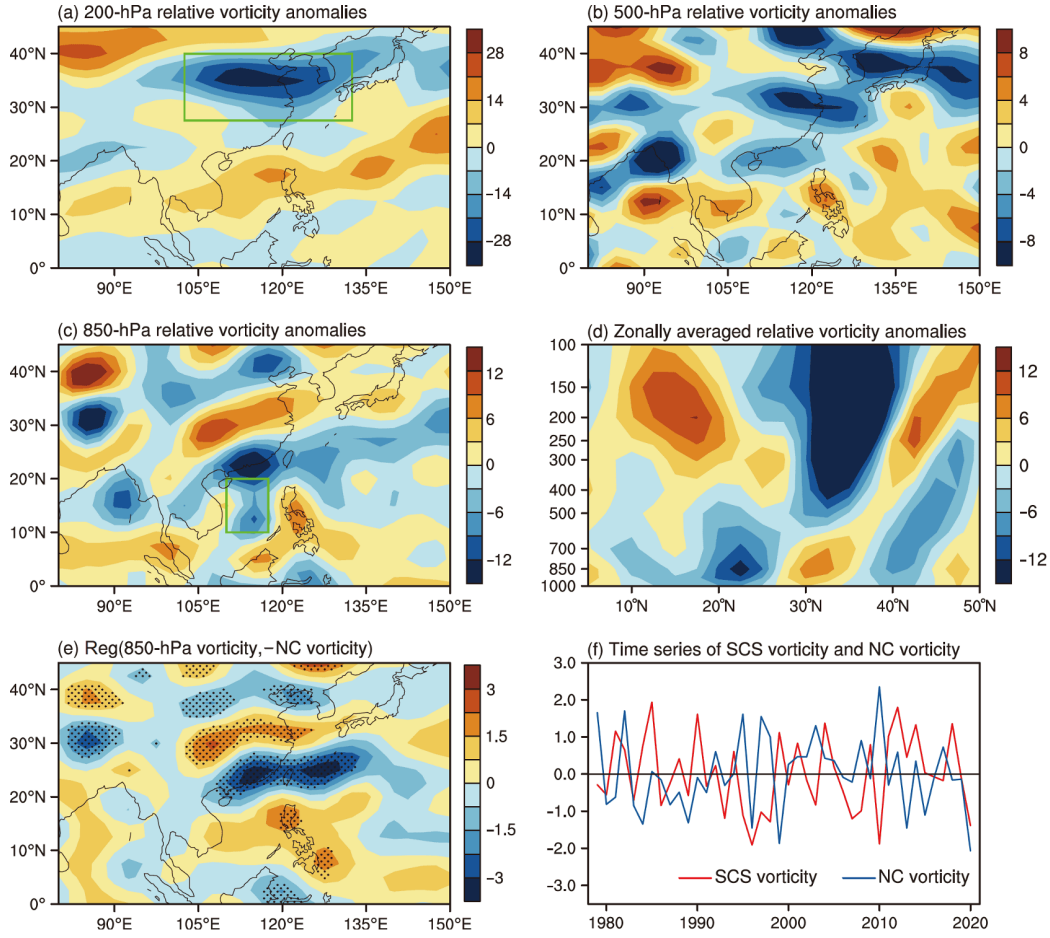

Figure 3 Relative vorticity anomalies in June 2020. (a) 200-hPa relative vorticity anomalies (unit: 10^{-6} s^{-1}) in June 2020. The green rectangle denotes the North China (NC) region (102.5°–132.5°E, 27.5°–40°N). (b) As in (a) but for 500-hPa. (c) As in (a) but for 850-hPa. The green rectangle denotes the region used to calculate the South China Sea (SCS) vorticity (110°–117.5°E, 10°–20°N). (d) Zonally averaged relative vorticity anomalies (unit: 10^{-6} s^{-1}) over the longitude band of 110°–117.5°E in June 2020. (e) June 850-hPa relative vorticity anomalies (shading, units: 10^{-6} s^{-1}) regressed onto the reversed NC vorticity. The areas significant at the 95% confidence level are dotted. (f) Standardized time series of the June SCS vorticity (red line) and June NC vorticity (blue line) during the 1979–2020 period. The SCS (NC) vorticity is defined as the June 850-hPa (200-hPa) relative vorticity averaged in the SCS (NC) region.

stronger than normal and is located west of the anomalous anticyclone, while enhanced rainfall anomalies are located on the northwest flank of the anomalous anticyclone. The correlation between the June rainfall in the YRV and the reversed NC (SCS) vorticity is 0.58 (0.28), which is significant (insignificant) at the 95% confidence level. It seems that the June rainfall in the YRV is largely controlled by the atmospheric process associated with the NC vorticity.

As shown in Figure 2f, there are stronger-than-normal meridional moisture flux anomalies over South China in June 2020. Upon comparisons of Figures 2f, 4c and 4d, stronger-than-normal meridional moisture transportation in the South China region (102.5°–112.5°E, 20°–30°N) in June 2020 should be the combined effect of the atmospheric processes associated with the SCS vorticity and NC vorticity. As shown in Figure 4e and 4f, the meridional moisture flux in South China is significantly related to both the SCS vorticity and the NC vorticity. In June 2020, the water vapor transportation enhanced by atmospheric process associated with negative SCS vorticity is further enhanced by atmospheric process associated with negative NC vorticity. Moreover, the water vapor is transported further northward due to the influence of negative NC vorticity, and result in positive rainfall anomalies in the YRV.

To confirm the combined effect of negative SCS vorticity and negative NC vorticity, a combined index for the co-existence of negative SCS vorticity and negative NC vorticity is simply defined by the standardized reversed SCS vorticity plus the standardized reversed NC vorticity. Figure 5a presents rainfall and moisture flux anomalies regressed onto the standardized combined index. The regressed rainfall anomalies are mainly located in the YRV, which is similar to Figure 4d, suggesting that the location of rainfall anomalies in June 2020 is primarily controlled by the NC vorticity. However, regressed positive rainfall anomalies in the YRV are much heavier when negative SCS vorticity and negative NC vorticity co-exist. Moreover, the June rainfall in the YRV has a closer relationship with the combined index than that

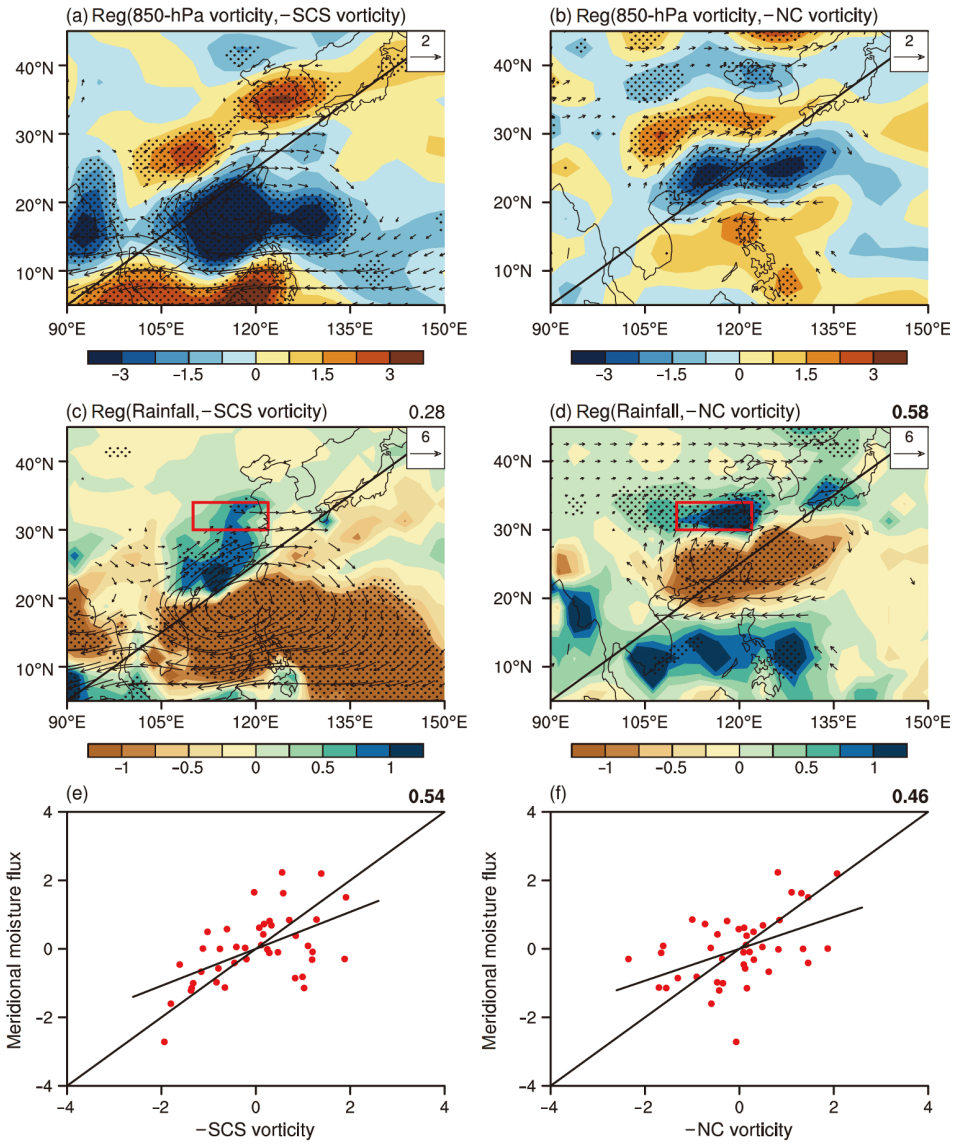

Figure 4 June rainfall and meridional moisture flux anomalies associated with the SCS vorticity and NC vorticity. (a) and (b) June 850-hPa relative vorticity anomalies (shading, units: 10^{-6} s^{-1}) and wind anomalies (vectors, units: m s^{-1}) regressed onto the reversed SCS vorticity and reversed NC vorticity. The areas of relative vorticity anomalies significant at the 95% confidence level are dotted, and the winds significant at the 95% confidence level are plotted. (c) and (d) As in (a) and (b) but for June rainfall anomalies (shading, unit: mm day^{-1}) and column-integrated moisture flux anomalies (vectors, unit: kg m^{-1} s^{-1}) regressed onto the reversed SCS vorticity and reversed NC vorticity. Red rectangles denote the YRV region. The correlation between the reversed SCS vorticity or reversed NC vorticity and the June rainfall in the YRV is given in the upper right corner, and the bold indicates significant at the 95% confidence level. (e) and (f) Scatter plot of the meridional moisture flux in South China (102.5°–112.5°E, 20°–30°N) versus the reversed SCS vorticity and reversed NC vorticity. Line of best fit is also shown, the correlation between the reversed SCS vorticity or reversed NC vorticity and the meridional moisture flux in South China is given in the upper right corner, and the bold indicates significant at the 95% confidence level.

with the NC vorticity, whereas the meridional moisture flux in South China has a closer relationship with the combined index than those with the SCS vorticity or the NC vorticity (Figure 5a and 5b). This finding suggests that the positive rainfall anomalies in the YRV induced by negative NC vorticity can be further enhanced by atmospheric process associated with negative SCS vorticity through providing favorable moisture conditions. Overall, these results imply that the atmospheric processes associated with both the SCS vorticity and NC vorticity play important roles in the record-breaking rainfall in June 2020. Thus, the SCS vorticity in the lower troposphere and NC vorticity in the upper troposphere are used as indicators to detect the ocean-atmosphere processes responsible for the June rainfall changes in the YRV.

3.2 Influences of El Niño and its capacitors on moisture transportation in South China

Figure 6a−6c presents SST anomalies in the preceding winter (D(−1)JF), preceding spring (MAM) and June regressed onto the reversed SCS vorticity during the study period. Clearly, the SCS vorticity is strongly related to the decaying phase of

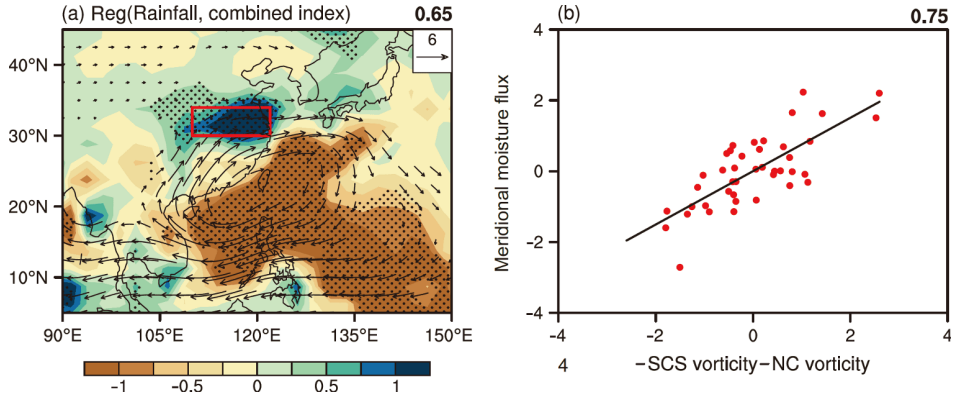

Figure 5 June rainfall and meridional moisture flux anomalies associated with the co-existence of negative SCS vorticity and negative NC vorticity. (a) and (b) As in Figure 4c and Figure 4e but for the combined index. The combined index is simply defined by the standardized reversed SCS vorticity plus the standardized reversed NC vorticity.

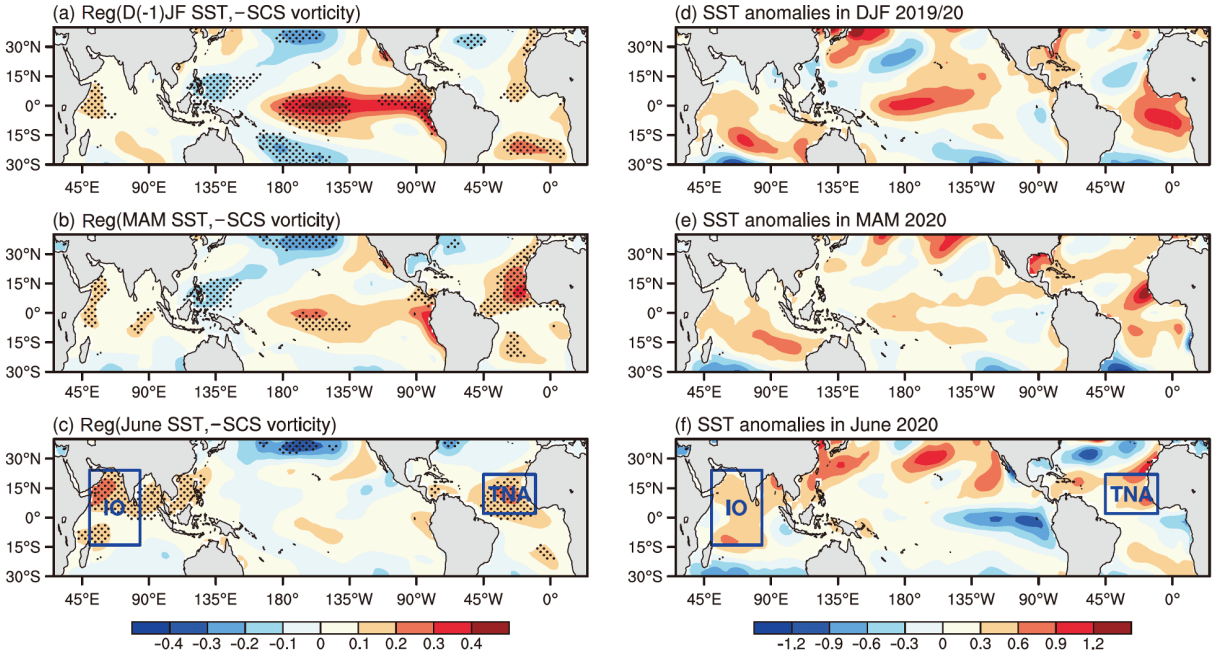

Figure 6 SST anomalies associated with the SCS vorticity. (a)−(c) D(−1)JF, MAM, and June SST anomalies (unit: °C) regressed onto the reversed SCS vorticity. The areas significant at the 95% confidence level are dotted. (d)−(f) SST anomalies (unit: °C) in DJF 2019/20, MAM 2020, and June 2020. The blue rectangles denote the Indian Ocean region (IO; 50°−84°E, 14°S−24°N) and the tropical North Atlantic region (TNA; 45°−10°W, 2°−22°N).

ENSO events. In the preceding winter, positive SST anomalies are located in the central Pacific, negative SST anomalies are over the western North Pacific. In the preceding spring, positive SST anomalies in the tropical North Atlantic (TNA) and Indian Ocean (IO) increase, when positive SST anomalies in the central Pacific decay. In June, positive SST anomalies in the IO and TNA become stronger, with the disappearance of negative SST anomalies in the western North Pacific. From the preceding winter 2019/20 to June 2020, the SST anomalies also exhibit similar patterns (Figure 6d−6f). These results indicate that the IO and TNA act as capacitors to prolong the effect of Pacific ENSO events on atmospheric circulation anomalies in the western North Pacific, which is consistent with previous studies (Xie et al., 2009; Wang et al., 2017).

To confirm the effect of El Niño's capacitors (the IO and TNA) on moisture transportation in South China, Figure 7 shows the June 850-hPa wind anomalies, rainfall anomalies and moisture flux anomalies regressed onto the June IO SST and June TNA SST. The IO SST is calculated as the average SST over the region (50°−84°E, 14°S−24°N), whereas the TNA SST is defined as the average SST over the region (45°−10°W, 2°−22°N). It shows that positive SST anomalies in the IO and TNA can induce an anomalous anticyclone and negative relative vorticity anomalies in the SCS, enhance water vapor transportation from the SCS to South China, and

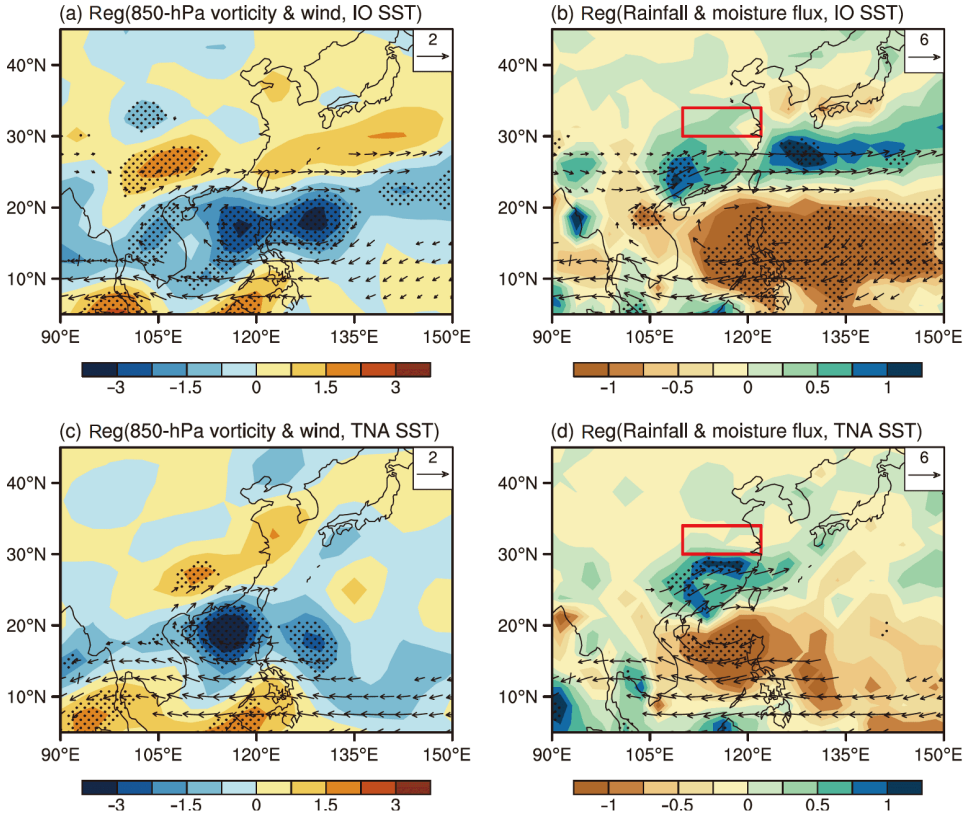

Figure 7 June atmospheric circulation and rainfall anomalies associated with the June IO SST and June TNA SST. (a) and (c) June 850-hPa relative vorticity anomalies (shading, units: 10^{-6} s^{-1}) and horizontal wind anomalies (vectors, units: m s^{-1}) regressed onto the June IO SST and June TNA SST. The areas of relative vorticity anomalies significant at the 95% confidence level are dotted, and the winds significant at the 95% confidence level are plotted. (b) and (d) As in (a) and (c) but for the June rainfall anomalies (shading, unit: mm day^{-1}) and column-integrated moisture flux anomalies (vectors, unit: kg m^{-1} s^{-1}). Red rectangles denote the YRV region.

lead to positive rainfall anomalies in South China. Although the locations of regressed rainfall anomalies in Figure 7 are outside of the YRV region, positive SST anomalies over the IO and TNA in June can enhance the meridional moisture flux in South China.

The question is how the June IO SST and June TNA SST affect the atmospheric circulation in the western North Pacific. Figure 8a shows the tropospheric (850−250 hPa) temperature anomalies regressed onto the June IO SST during the study period. The warm SST in the IO can heat the whole troposphere in the IO, emanate an atmospheric Kelvin wave into the Pacific, and result in an anomalous anticyclone in the western North Pacific, which is consistent with the results in Xie et al. (2009). For the June SST in the TNA, Figure 8b presents the tropospheric temperature anomalies regressed onto the June TNA SST. The warm SST in the TNA can also induce an atmospheric Kelvin wave into the Pacific, and favor the formation of an anomalous anticyclone in the western North Pacific, which is similar to the results in Lu and Dong (2005) and Rong et al. (2010). These results show that, with the IO and TNA as capacitors, Pacific El Niño events in the preceding winter can induce an anomalous anticyclone in the western North Pacific, and lead to enhanced water vapor transportation in South China.

3.3 Influence of preceding May western North Atlantic SST on rainfall in the YRV

Figure 9 shows the 200-hPa GPH anomalies and horizontal wave-activity fluxes associated with the NC vorticity. As shown in Figure 9a, there is a wave train with alternating positive and negative GPH anomalies in the middle-high latitudes of the Atlantic-Eurasian continent region, suggesting that the NC vorticity is mainly controlled by atmospheric processes in the middle to high latitudes. In particular, there are strong positive GPH anomalies in the mid-latitude North Atlantic (MNA, 52.5°–15°W, 42.5°–50°N). In June 2020, a wave train with alternating positive and negative GPH anomalies also exists in the middle-high latitudes of the Atlantic-Eurasian continental region (Figure 9b). Figure 9c and 9d shows that the positive GPH anomalies in the MNA can significantly affect the rainfall in the YRV through atmospheric wave train. Based on the standardized time series of the MNA GPH in Figure 9e, the MNA GPH in June 2020 is record-breaking since 1979. This record-breaking positive GPH anomalies in the MNA can emanate an atmospheric wave train in the middle-high latitudes of the Atlantic-Eurasian continental region and lead to enhanced rainfall in the YRV.

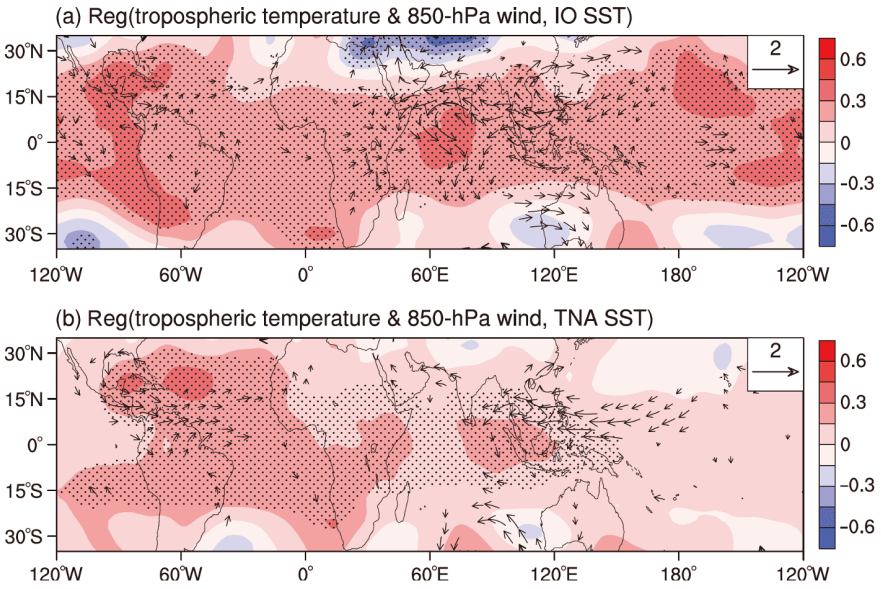

Figure 8 Physical processes involved in the influences of the June IO SST and June TNA SST on the atmospheric circulation in the western North Pacific. (a) Tropospheric (850−250 hPa) temperature anomalies (shading, unit: °C) and 850-hPa wind anomalies (vectors, unit: m s^{-1}) regressed onto the June IO SST. The areas of tropospheric temperature anomalies significant at the 95% confidence level are dotted, and the winds significant at the 95% confidence level are plotted. (b) As in (a) but for the June TNA SST.

To detect whether the positive GPH in the MNA is forced by the SST, Figure 10a shows the June SST anomalies regressed onto the June MNA GPH. Positive SST anomalies are located in the MNA, and negative SST anomalies are located to the north and south of the MNA, forming a tripole pattern, which is different from the North Atlantic tripole related to the North Atlantic Oscillation (Wu et al., 2009). SST anomalies in June 2020 also show a tripole pattern (Figure 10b). This tripole pattern of SST anomalies is forced by atmospheric circulation, although it may provide feedback on atmospheric circulation. Hence, we focus on the relationship between the June MNA GPH and preceding May SST. Figure 10c shows that the June MNA GPH is strongly related to the May SST anomalies in the western North Atlantic (WNA; 80°–52°W, 18°–28°N). In May 2020, a band of extremely positive SST anomalies also exist in the WNA (Figure 10d). The average SST in the WNA in May 2020 is also record-breaking since 1979 (Figure S4). As shown in Figure 10e and 10f, this extremely warm WNA SST in May can induce extremely positive June GPH anomalies in the MNA, which lead to positive rainfall anomalies in the YRV through atmospheric wave train. This finding suggests that the MNA GPH acts as a bridge between the May SST in the WNA and the June rainfall anomalies in the YRV, and the May SST in the WNA is a good predictor of the June rainfall anomalies in the YRV.

4. Conclusions and discussions

In summary, record-breaking rainfall occurred over the YRV in June 2020. The SST anomalies in all three oceans of the Pacific, Indian and Atlantic Oceans contribute to this record-breaking rainfall over the YRV, but the Atlantic seems to play a dominant role. Figure 11 shows the schematic diagram of physical processes responsible for strong positive rainfall anomalies over the YRV in June 2020. Associated with the SST anomalies of three oceans are negative 200-hPa relative vorticity anomalies in NC and negative 850-hPa relative vorticity anomalies over the SCS in June 2020. Both of these two vorticity anomalies contribute to the rainfall in the YRV, but the rainfall anomalies in the YRV are mainly controlled by the atmospheric process associated with the NC vorticity. However, rainfall anomalies in the YRV can be further enhanced by atmospheric process associated with negative SCS vorticity by providing favorable moisture conditions. Further analyses show that the positive May SST anomalies in the western North Atlantic induce positive GPH anomalies over the the mid-latitude North Atlantic in June, which affect the NC vorticity and the rainfall anomalies in the YRV by atmospheric wave train across the European continent. The IO and TNA SSTs, as capacitors of Pacific El Niño events, induce negative relative vorticity anomalies over the SCS in June, which also affect rainfall in the YRV by increasing the moisture transport to the YRV region. Thus, all three oceans make contributions to the rainfall over the YRV in June 2020, but the Atlantic plays a dominant role.

Previous studies have focused on the influence of tropical and subtropical factors on summer rainfall variations over China. Here, we found that the co-existence of negative SCS vorticity and negative NC vorticity contributed to the June record-breaking rainfall in the YRV. Atmospheric processes

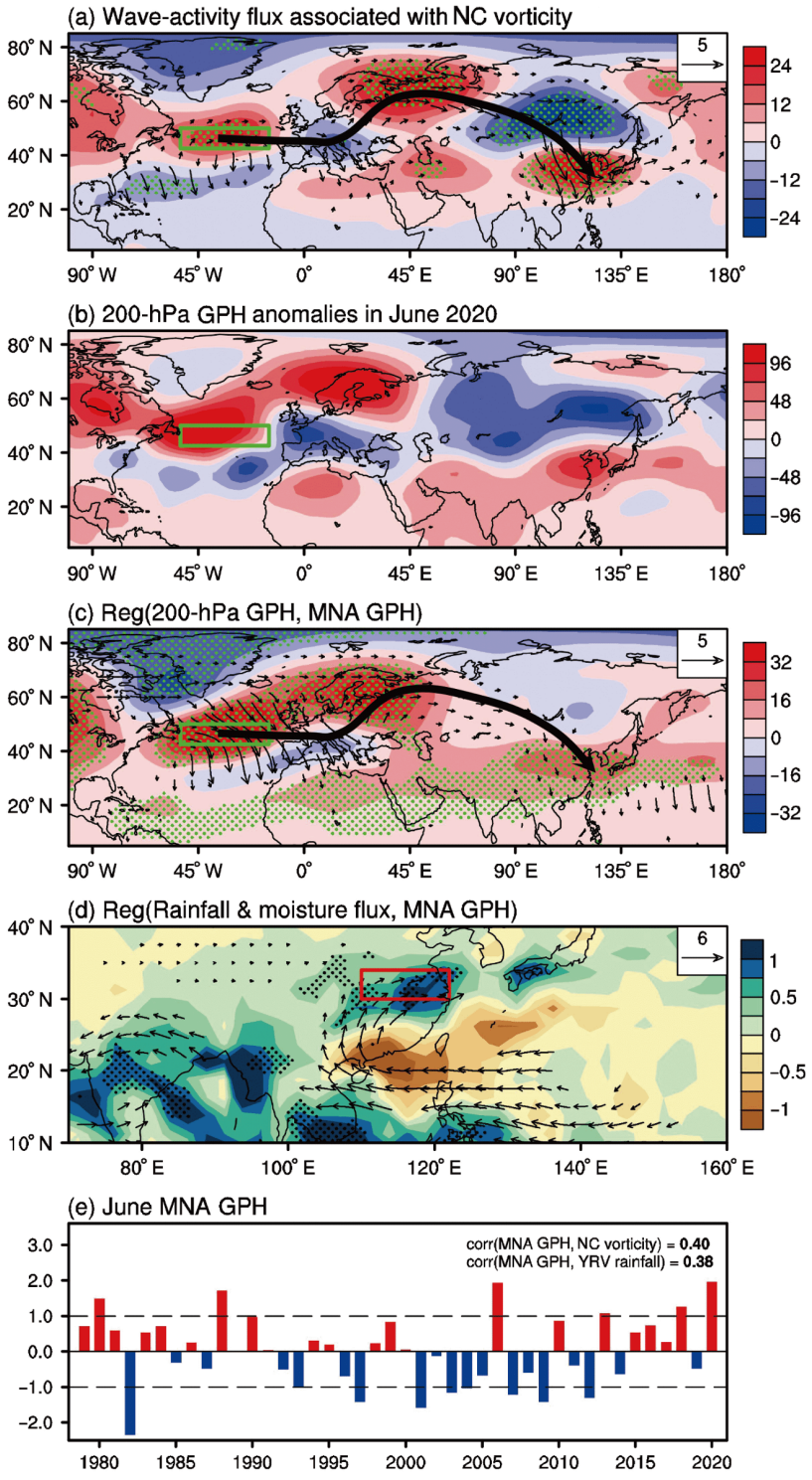

Figure 9 Influence of the mid-latitude North Atlantic (MNA) GPH on the rainfall in the YRV region. (a) June 200-hPa GPH anomalies (shading, unit: gpm) regressed onto the NC vorticity. The areas significant at the 95% confidence level are dotted. The horizontal wave-activity fluxes (vectors, units: 10^{-1} m^2 s^{-2}, omitted below 0.05 m^2 s^{-2}) and schematic wave train (thick arrowed line) associated with the NC vorticity are also shown. The green rectangle denotes the MNA region (52.5°–15°W, 42.5°–50°N). (b) 200-hPa GPH anomalies (unit: gpm) in June 2020. (c) As in (a) but for the MNA GPH. (d) June rainfall anomalies (shading, unit: mm day^{-1}) and column-integrated moisture flux anomalies (vectors, unit: kg m^{-1} s^{-1}) regressed onto the MNA GPH. The areas of rainfall anomalies significant at the 95% confidence level are dotted, and the vectors significant at the 95% confidence level are plotted. The red rectangle denotes the YRV region. (e) Standardized time series of the June MNA GPH during the 1979–2020 period.

associated with the SCS vorticity and mid-latitude wave train associated with the NC vorticity can be forced by three-ocean SSTs. Additionally we found that May SST in the WNA is a good predictor the June rainfall anomalies in the

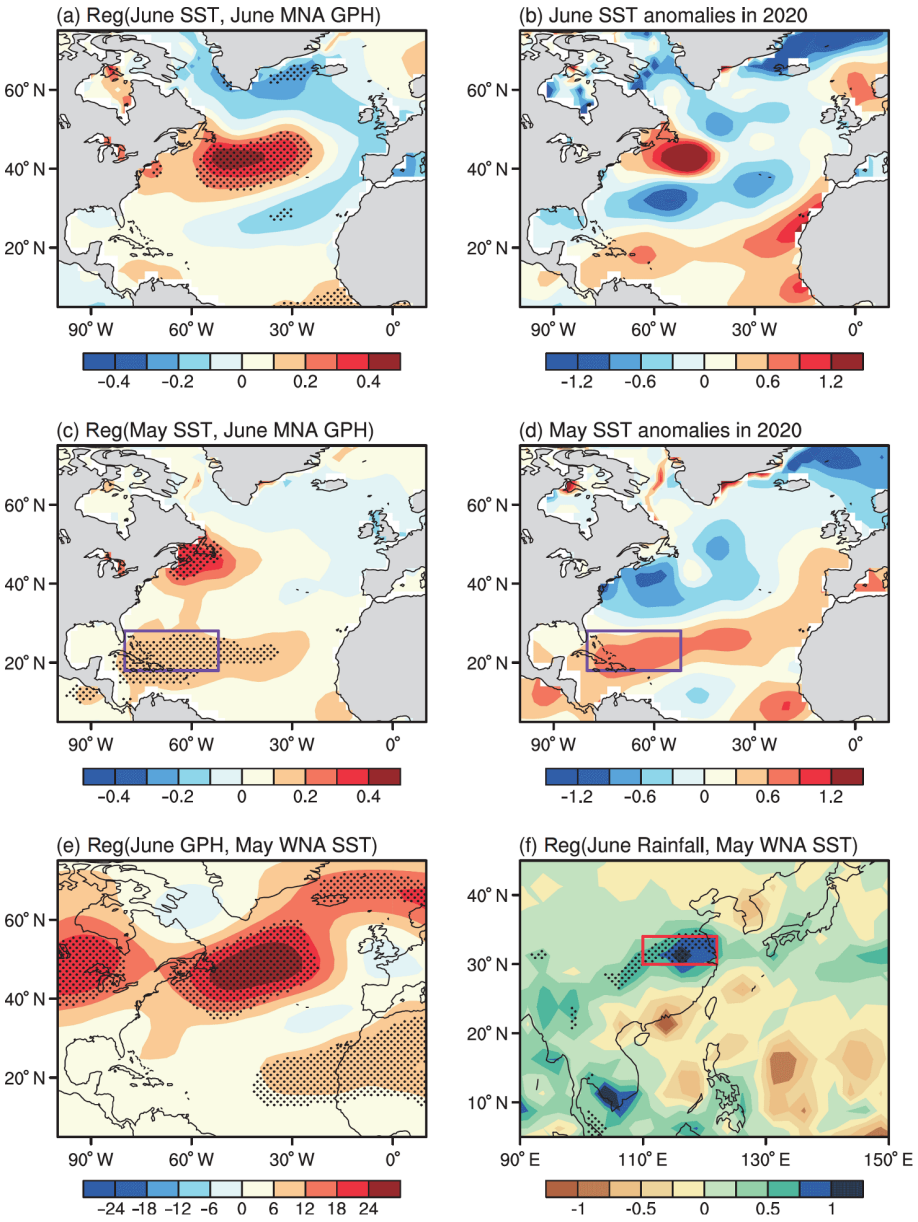

Figure 10 Influence of May SST in the western North Atlantic (WNA) on the June MNA GPH and rainfall anomalies in the YRV. (a) June SST anomalies (unit: °C) regressed onto the June MNA GPH. The areas significant at the 95% confidence level are dotted. (b) SST anomalies (unit: °C) in June 2020. (c) As in (a) but for May SST anomalies regressed onto the June MNA GPH. (d) As in (b) but for May SST anomalies. Purple rectangles in (c, d) denote the WNA region (80°–52°W, 18°–28°N). (e) As in (a) but for 200-hPa June GPH anomalies (unit: gpm) regressed onto the May SST in the WNA. (f) As in (a) but for June rainfall anomalies (unit: mm day^{-1}) regressed onto May SST in the WNA. The red rectangle denotes the YRV region.

YRV. This study not only promotes the understanding of June rainfall in the YRV but also highlights the importance of three-ocean SSTs in extreme weather and climate events.

We emphasize in this study that negative NC vorticity and negative SCS vorticity have a combined influence on the extremely heavy rainfall over the YRV in June 2020. However, we do not downplay other climate phenomena that may also play roles in the rainfall over the YRV. For example, it is found that above-normal rainfall in June 1991 is possibly due to the negative 850-hPa relative vorticity anomalies over the south of Japan and Indochina Peninsula (figure not shown). Another question is how the co-existence of negative NC vorticity and negative SCS vorticity affects summer (June-August) rainfall in China. As shown in Figure S5, negative SCS (NC) vorticity significantly affect summer rainfall in the YRV (the north of China), whereas the co-existence of negative NC vorticity and negative SCS vorticity favors positive rainfall anomalies in the region from the YRV to the north of China. Especially, positive summer rainfall anomalies in the north of China induced by negative NC vorticity can also be further enhanced by negative SCS vorticity. More details on the physical processes contributing

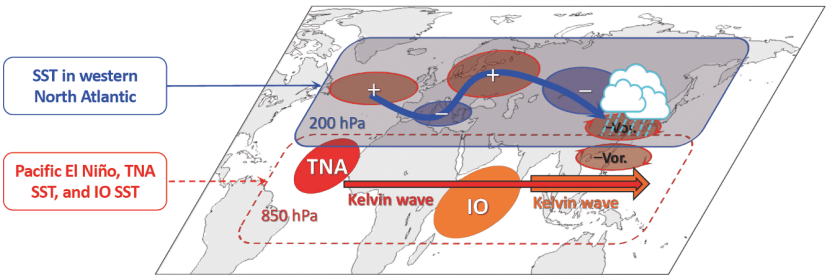

Figure 11 Schematic diagram of physical processes responsible for heavy rainfall anomalies over the Yangtze River Valley in June 2020. –Vor.: negative relative vorticity anomalies; "+": positive 200-hPa geopotential height (GPH) anomalies; "–": negative 200-hPa GPH anomalies; blue arrowed line: atmospheric wave train across Europe and reaching Asia; IO: Indian Ocean; TNA: tropical North Atlantic. The Atlantic induces positive GPH anomalies in the mid-latitude North Atlantic, which affect the North China vorticity via atmospheric wave train across Europe, whereas the IO and TNA SSTs (capacitors of Pacific El Niño events) are associated with the South China Sea vorticity. The combined effect of the North China vorticity and the South China Sea vorticity induces a heavy rainfall over the Yangtze River Valley. All of three oceans contribute to the rainfall over the Yangtze River Valley in June 2020, but the Atlantic plays a dominant role.

to extremely strong rainfall in China should be further investigated in future studies.

Acknowledgements *We thank two reviewers whose comments and suggestions help improve the manuscript. This study was supported by the National Key R&D Program of China (Grand No. 2019YFA0606701), the National Natural Science Foundation of China (Grand No. 41731173), the Strategic Priority Research Program of the Chinese Academy of Sciences (Grand Nos. XDB42000000 & XDA20060502), the Key Special Project for Introduced Talents Team of Southern Marine Science and Engineering Guangdong Laboratory (Guangzhou) (Grand No. GML2019ZD0306), the Innovation Academy of South China Sea Ecology and Environmental Engineering, the Chinese Academy of Sciences (Grand No. ISEE2018PY06), the Leading Talents of Guangdong Province Program, the National Program on Global Change and Air-Sea Interaction under grant GASI-IPOVAI-03, and the Independent Research Project Program of State Key Laboratory of Tropical Oceanography (Grand No. LTOZZ2004). The numerical computation was supported by the High Performance Computing Division in the South China Sea Institute of Oceanology.*

References

Chen M, Xie P, Janowiak J E, Arkin P A. 2002. Global land precipitation: A 50-yr monthly analysis based on gauge observations. J Hydrometeor, 3: 249–266

Chen Z, Du Y, Wen Z, Wu R, Xie S P. 2019. Evolution of south tropical Indian Ocean warming and the climatic impacts following strong El Niño events. J Clim, 32: 7329–7347

Ding R, Ha K J, Li J. 2010. Interdecadal shift in the relationship between the East Asian summer monsoon and the tropical Indian Ocean. Clim Dyn, 34: 1059–1071

Ding Y, Chan J C L. 2005. The East Asian summer monsoon: An overview. Meteorol Atmos Phys, 89: 117–142

Ding Y, Liang P, Liu Y, Zhang Y. 2020. Multiscale variability of Meiyu and its prediction: A new review. J Geophys Res Atmos, 125: e31496

Huang B, Thorne P W, Banzon V F, Boyer T, Chepurin G, Lawrimore J H, Menne M J, Smith T M, Vose R S, Zhang H M. 2017. Extended reconstructed sea surface temperature, version 5 (ERSSTv5): Upgrades, validations, and intercomparisons. J Clim, 30: 8179–8205

Kalnay E, Kanamitsu M, Kistler R, Collins W, Deaven D, Gandin L, Iredell M, Saha S, White G, Woollen J, Zhu Y, Leetmaa A, Reynolds R, Chelliah M, Ebisuzaki W, Higgins W, Janowiak J, Mo K C, Ropelewski C, Wang J, Jenne R, Joseph D. 1996. The NCEP/NCAR 40-year reanalysis project. Bull Amer Meteor Soc, 77: 437–472

Li J, Zeng Q. 2002. A unified monsoon index. Geophys Res Lett, 29: 115-1–115-4

Liu B, Yan Y, Zhu C, Ma S, Li J. 2020. Record-Breaking Meiyu Rainfall Around the Yangtze River in 2020 Regulated by the Subseasonal Phase Transition of the North Atlantic Oscillation. Geophys Res Lett, 47: e90342

Lu R. 2002. Indices of the summertime western North Pacific subtropical high. Adv Atmos Sci, 19: 1004–1028

Lu R, Dong B. 2005. Impact of Atlantic sea surface temperature anomalies on the summer climate in the western North Pacific during 1997–1998. J Geophys Res, 110: D16102

Lu R, Ying L, Ryu C S. 2008. Relationship between the zonal displacement of the western Pacific subtropical high and the dominant modes of low-tropospheric circulation in summer. Prog Nat Sci, 18: 161–165

Nan S, Li J. 2003. The relationship between the summer precipitation in the Yangtze River valley and the boreal spring Southern Hemisphere annular mode. Geophys Res Lett, 30: 2266

Rong X Y, Zhang R H, Li T. 2010. Impacts of Atlantic sea surface temperature anomalies on Indo-East Asian summer monsoon-ENSO relationship. Chin Sci Bull, 55: 2458–2468

Sun J, Ming J, Zhang M, Yu S. 2018. Circulation features associated with the record-breaking rainfall over South China in June 2017. J Clim, 31: 7209–7224

Takaya Y, Ishikawa I, Kobayashi C, Endo H, Ose T. 2020. Enhanced Meiyu-Baiu rainfall in early summer 2020: Aftermath of the 2019 super IOD event. Geophys Res Lett, 47: 1–9

Takaya K, Nakamura H. 2001. A formulation of a phase-independent wave-activity flux for stationary and migratory quasigeostrophic eddies on a zonally varying basic flow. J Atmos Sci, 58: 608–627

Wang C. 2019. Three-ocean interactions and climate variability: A review and perspective. Clim Dyn, 53: 5119–5136, doi: 10.1007/s00382-019-04930-x

Wang L, Gu W. 2016. The Eastern China flood of June 2015 and its causes. Sci Bull, 61: 178–184

Wang L, Yu J Y, Paek H. 2017. Enhanced biennial variability in the Pacific due to Atlantic capacitor effect. Nat Commun, 8: 14887

Wu Z, Wang B, Li J, Jin F F. 2009. An empirical seasonal prediction model of the East Asian summer monsoon using ENSO and NAO. J Geophys Res, 114: D18120

Xie P, Arkin P A. 1997. Global precipitation: A 17-year monthly analysis based on gauge observations, satellite estimates, and numerical model outputs. Bull Amer Meteor Soc, 78: 2539–2558

Xie S P, Hu K, Hafner J, Tokinaga H, Du Y, Huang G, Sampe T. 2009. Indian Ocean capacitor effect on Indo–western Pacific climate during the summer following El Niño. J Clim, 22: 730–747

Yang H, Sun S. 2005. The characteristics of longitudinal movement of the subtropical high in the western Pacific in the pre-rainy season in South China. Adv Atmos Sci, 22: 392–400

Yuan C, Liu J, Luo J J, Guan Z. 2019. Influences of tropical Indian and Pacific oceans on the interannual variations of precipitation in the early and late rainy seasons in South China. J Clim, 32: 3681–3694

(Responsible editor: Xiuqun YANG)